

Supporting Information

Interfacial Engineering Approach towards Two-Dimensional Porous Carbon Hybrids for High Performance Energy Storage and Conversion

Chenbao Lu, Shaohua Liu, Fan Zhang,* Yuezeng Su,* Xiaoxin Zou, Zhan Shi, Guodong Li, Xiaodong Zhuang*

C. Lu, Prof. Y. Su

School of Aeronautics and Astronautics and School of Electronic Information and Electrical Engineering, Shanghai Jiao Tong University, 200240 Shanghai, P. R. China, E-mail: yzsu@sjtu.edu.cn

Prof. F. Zhang, Dr. S. Liu, Dr. X. Zhuang

Shanghai Key Lab of Electrical Insulation and Thermal Ageing & Shanghai Electrochemical Energy Devices Research Center, School of Chemistry and Chemical Engineering, Shanghai Jiao Tong University, 200240 Shanghai, P. R. China, E-mail: fan-zhang@sjtu.edu.cn; zhuang@sjtu.edu.cn

Prof. X. Zou, Prof. Z. Shi, Prof. G. Li

State Key Laboratory of Inorganic Synthesis and Preparative Chemistry, International Joint Research Laboratory of Nano-Micro Architecture Chemistry, College of Chemistry, Jilin University, Changchun 130012, P. R. China

Dr. X. Zhuang

Center for Advancing Electronics Dresden (cfaed) & Department of Chemistry and Food Chemistry, Technische Universität Dresden, Mommsenstrasse 4, Dresden 01062, Germany

Supporting information

Contents:

1. Experimental details.
2. Figure S1. Digital photos of the interfacial polymerization in large scale.
3. Figure S2. SEM and TEM images of PANI nanofibers.
4. Figure S3. XRD patterns and FT-IR spectra of GO@PANI nanosheets, PANI nanofibers, and GO nanosheets.
5. Figure S4. SEM and TEM images of GO@PANI fabricated at different GO/aniline weight ratio.
6. Figure S5. AFM survey of GO@PANI fabricated at different GO/aniline weight ratio.
7. Figure S6. SEM and TEM images of GO@(B@PANI).
8. Figure S7. SEM and TEM images of GO@(Te@PANI).
9. Figure S8. SEM and TEM image of GO@(Fe@P@PANI).
10. Figure S9. Enlarged SEM and TEM image of GO@(Fe₂P@NPC).
11. Figure S10. SEM images of pure Fe₂P nanoparticles.
12. Figure S11. XRD patterns of RG@(Fe₂P@NPC) and Fe₂P nanoparticles.
13. Figure S12. XPS survey spectra of RG@(Fe₂P@NPC) and Fe₂P nanoparticles.
14. Figure S13. N₂ sorption isotherms of RG@(Fe₂C@NPC), RG@NPC, and NPC.
15. Figure S14-16. XRD patterns of RG@(MoP@NPC), RG@(Co₂P@NPC), RG@(Ni₁₂P₅@NPC).
16. Figure S17. Supercapacitor performance of RG@(Fe₂P@NPC).
17. Figure S18. CV and galvanostatic charge-discharge curves for NPC, RG@NPC, and Fe₂P nanoparticles.
18. Figure S19. Nyquist plots of the NPC, RG@NPC, Fe₂P nanoparticles, and RG@(Fe₂P@NPC).
19. Figure S20. HER performance of the RG@(Fe₂P@NPC) in 0.5 M H₂SO₄.
20. Figure S21. Equivalent circuit used for fitting of EIS data.
21. Figure S22. XRD pattern of RG@(Fe₂P@Co₂P@NPC).
22. Figure S23. XPS spectra of RG@(Fe₂P@Co₂P@NPC).
23. Figure S24. CV curves for RG@NPC and RG@(MP@NPC)s, recorded under N₂ saturated and O₂ saturated 0.1 M KOH solutions.
24. Figure S25. RRDE current-potential curves for RG@NPC and RG@(MP@NPC)s for ORR in O₂ saturated 0.1 M KOH solution.
25. Figure S26. ORR performance of RG@(Fe₂P@Co₂P@NPC).
26. Figure S27. XRD pattern of RG@(Fe₃C@NPC).
27. Table S1. Elemental analysis of C, N, O, P, Fe, and Co based on XPS analysis.
28. Table S2. N₂ sorption data for RG@(Fe₂P@NPC), RG@NPC, and NPC.
29. Table S3. Comparison of supercapacitor performance of reported porous carbons or metal phosphides based nanomaterials.
30. Table S4. The charge-transfer resistance values (R_{ct}) of the samples in 6 M KOH.
31. Table S5. The R_{ct} of MPs-base carbon nanosheets in 0.5 M H₂SO₄.
32. Table S6. Comparison of HER performance in acid media for as-prepared MPs-based catalysts.
33. Table S7. Comparison of HER performance in acid media for RG@(Fe₂P@NPC) with other HER electrocatalysts.

Experimental section:

Chemicals: $\text{FeCl}_3 \cdot 6\text{H}_2\text{O}$, $\text{CoCl}_2 \cdot 6\text{H}_2\text{O}$, $\text{Ni}(\text{OAc})_2 \cdot 4\text{H}_2\text{O}$, $(\text{NH}_4)_2\text{Mo}_4\text{O}_{13} \cdot 2\text{H}_2\text{O}$ and aniline were purchased from Aladdin Reagent Co. Ammonium peroxydisulfate (APS), HCl (36 wt.%), H_3PO_4 (80%), H_2SO_4 (98%), KMnO_4 , NaNO_3 , and H_2O_2 were purchased from Sinopharm Chemical Reagent Co. Pt/C (20 wt.%) were purchased from Sigma-Aldrich. Nafion solution (0.5 wt.%) was purchased from DuPont, Ltd. All chemicals were used without further purification. All aqueous solutions were prepared with DI water.

Interfacial preparation of GO@PANI. Typically, the interfacial reaction was performed in a 20 mL glass vial. Firstly, ammonium peroxydisulfate (APS, 245 mg, 1 mmol) was dissolved in 8 mL of 1 M dopant acid (HCl) solution. Then, 2 mL of aqueous GO dispersion (2.5 mg mL^{-1}) which was synthesized by a modified Hummers method^[1] slowly added to the acid solution, followed by ultrasonication for 30 min to form a homogeneous suspension, as the aqueous layer. Subsequently, 100 μL aniline was dissolved in the organic phase (10 mL) toluene, as the organic layer. Then, organic phase was added carefully on the top of the aqueous solution, forming an organic/aqueous interface. The steady interface was standing 6 hours at room temperature. The 2D GO@PANI (1:20) was obtained after centrifuged and washed with DI water and ethanol. The GO@PANI (1:10) and GO@PANI (1:40) were synthesized by the same procedure with different weight ratio of GO to aniline.

For preparation of H_3BO_3 doped PANI nanosheet (GO@(B@PANI)), H_3PO_4 doped PANI nanosheet (GO@(P@PANI)) and H_6TeO_6 doped PANI nanosheet (GO@(Te@PANI)), the same procedure was employed by just using H_3BO_3 , H_3PO_4 and H_6TeO_6 as the doped acids, respectively.

Preparation of metal phosphide anchored N-doped porous carbon nanosheets (RG@(MP@NPC)s). Typically, Fe^{3+} and PO_4^{3-} anchored PANI nanosheet (GO@(Fe|P@PANI)) was firstly prepared by FeCl_3 and H_3PO_4 involved interfacial polymerization. First, 245 mg APS, 2 mL GO solution, and 1.5 g $\text{FeCl}_3 \cdot 6\text{H}_2\text{O}$ were added into the 8 mL of 1 M phosphoric acid aqueous solution. Subsequently, 100 μL aniline was dissolved in 10 mL toluene as the organic layer. The organic phase was added carefully on the top of the aqueous solution, forming an organic/aqueous interface. After reacting for 6 h, GO@(Fe|P@PANI) can be obtained after drying. After thermal treatment of GO@(Fe|P@PANI) under hydrogen/argon (5%) atmosphere at 1000 °C for 2 h,

RG@(Fe₂P@NPC) can be yield.

Synthetic routes for RG@(Co₂P@NPC), RG@(Ni₁₂P₅@NPC), and RG@(MoP@NPC) are similar to that for RG@(Fe₂P@NPC) by replacing FeCl₃ to corresponding transition metal salts (CoCl₂, Ni(OAc)₂ and (NH₄)₂Mo₄O₁₃). For preparation of Fe₂P and Co₂P anchored NPC nanosheet (RG@(Fe₂P|Co₂P@NPC)), the same procedure was used by adding both FeCl₃·6H₂O (800 mg) and CoCl₂·6H₂O (800 mg) into the aqueous solution.

Characterization:

SEM measurements were performed on a FEI Sirion-200 field emission scanning electron microscope. Transmission electron microscopy (TEM) images were acquired using a Tecnai G2 F20 S-TWIN transmission electron microscope (FEI) operated at 200 kV. AFM images of the materials on a freshly cleaved mica surface were taken with a Nanoscope III in tapping mode using a NSC14/no Alprobe (MikroMash, Wilsonville, Oregon). XRD analysis was performed on a RigakuD/Max 2500 X-ray diffractometer with Cu K α radiation ($\lambda=1.54\text{\AA}$) at generator voltage of 40 kV and a generator current of 50 mA with a scanning speed of 6 ° min⁻¹ over the range 5-80 (2 θ). FT-IR spectroscopy was performed on a Spectrum 100 (Perkin Elmer, Inc., USA) spectrometer with a scan range of 4000–400 cm⁻¹. X-ray photoemission spectroscopy (XPS) measurements were performed on a PHI-5000C ESCA system, the C 1s value was set at 284.6 eV for charge corrections. The gas sorption isotherms were measured via an Auto-sorb-iQA3200-4 sorption analyzer (Quantatech Co., USA) based on N₂ adsorption/desorption.

Electrochemical measurements.

Supercapacitor. The working electrodes were prepared by mixing as-prepared materials, carbon black (Super-P), and polytetrafluoroethylene (PTFE) at a weight ratio of 80:10:10 and pressed on platinum net. The area of the active material on each electrode was about 1.0 cm \times 0.5 cm (about 0.5 mg). The electrochemical capacitive of materials was evaluated in a three-electrode system, applying 6 M KOH as electrolyte, platinum wire and Ag/AgCl (saturated KCl) electrode as the counter and reference electrodes, respectively. The electrochemical performance of samples was determined by the cyclic voltammetry (CV) and galvanostatic charge-discharge. All electrochemical experiments were carried out at room temperature.

Electrochemical catalyzed HER. The electrodes were prepared as follows: 5 mg catalyst was blended with 50 μ l Nafion solution (0.5 wt %) and 450 μ l ethanol under sonication for 2h, producing

catalyst ink. Then 12 μl catalyst ink was pipetted on the surface of pre-polished glass carbon electrode (0.2471 cm^2). The electrodes were dried at room temperature before measurement. The HER experiments were performed in a three-electrode electrochemical cell at ambient temperature with a 660D CH Instrument potentiostat. An Ag/AgCl (KCl, 3 M) electrode as the reference electrode, and a carbon rod as the counter-electrode, respectively. The Ag/AgCl reference electrode was calibrated with respect to reversible hydrogen electrode (RHE). Linear sweep voltammetry (LSV) measurements were conducted in 0.5 M H_2SO_4 with scan rate of 5 mV s^{-1} . All the potentials reported in our work were vs. RHE. In 0.5 M H_2SO_4 , $E(\text{RHE}) = E(\text{Ag/AgCl}) + 0.214\text{ V}$, where E is the potential of the electrode. Electrochemical impedance spectroscopy (EIS) measurements were also carried out in the frequency range of 1000 kHz–0.02 Hz.

Electrochemical catalyzed ORR. The electrodes were prepared as follows: 5 mg catalyst was blended with 500 μl Nafion solution (0.05 wt %) and sonication for 2h, producing catalyst ink. Then 9 μl catalyst ink was pipetted on the surface of pre-polished glass carbon electrode (0.2471 cm^2). The electrodes were dried at room temperature before measurement. The ORR experiments were carried out in a conventional three electrodes cell using Wave Driver 20 bipotentiostatic (Pine Instrument Company, USA) at room temperature. An Ag/AgCl (KCl, 3M) reference electrode and a platinum wire counter electrode were used in the measurement. All tests were conducted in 0.1 M KOH, and the potentials in this study refer to that of reversible hydrogen electrode (RHE). In 0.1 M KOH, $E(\text{RHE}) = E(\text{Ag/AgCl}) + 0.944\text{ V}$. CV was performed in the potential range of -0.95-0.05V vs Ag/AgCl reference electrode under a sweep rate of 100 mV s^{-1} . RDE and RRDE were measured in O_2 -saturated 0.1 M KOH at 1600 rpm at a sweep rate of 10 mV s^{-1} .

The electron transfer number was determined by the following equation:

$$n=4I_d/(I_d+I_r/N) \quad (\text{S1})$$

The four electron selectivity of the catalysts was evaluated based on the H_2O_2 yield, calculated from the following equation:

$$\text{H}_2\text{O}_2(\%)=200I_r/N(I_d+I_r/N) \quad (\text{S2})$$

where I_D and I_R refer to disk current and ring current, respectively; and $N=0.37$ is the ring collection efficiency.

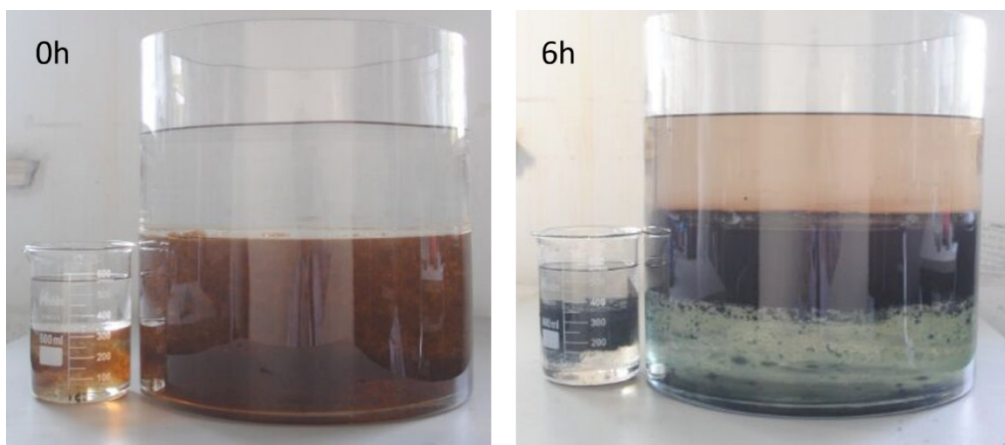


Fig. S1. Digital photos of the interfacial polymerization from 0 h (left) to 6 h (right) using 800 mL beaker and 25 L tank as reaction vessels. We can synthesis ~ 0.5 kg GO@PANI via such interfacial polymerization method each time, providing a general route to fabricate GO@PANI in large quantity.

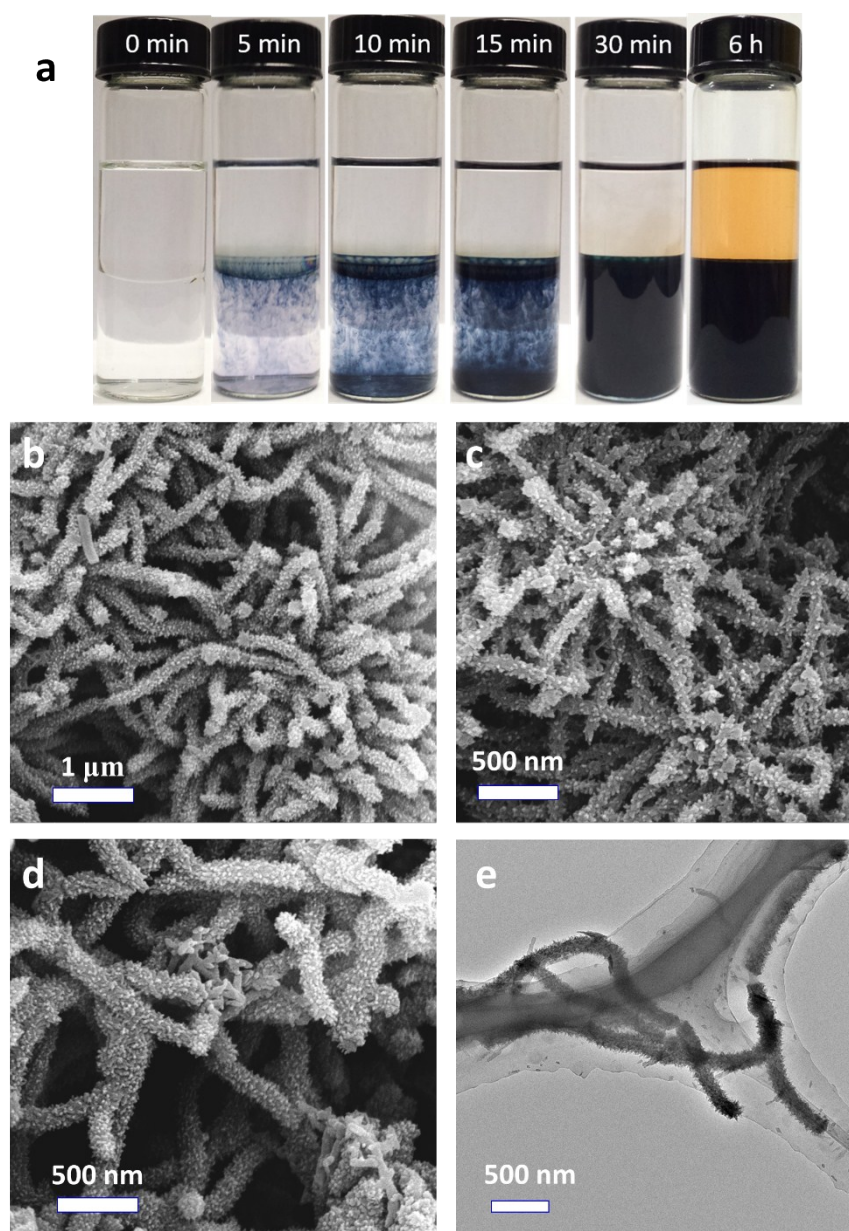


Fig. S2. (a) Digital photos of the interfacial polymerization without GO, from left to right the reaction times are 0 min, 5 min, 10 min, 15 min, 30 min and 6 h. The PANI diffusing downward due to the increased density, which consist of the presence of GO. (b-d) SEM and (e) TEM images of PANI nanofibers fabricated via interfacial polymerization of aniline without using GO.

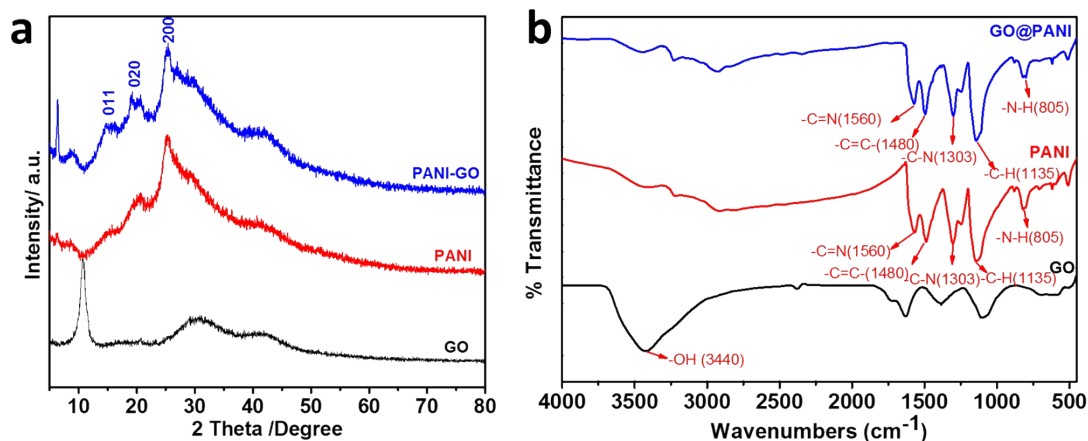


Fig. S3. (a) XRD patterns and (b) FT-IR spectra of GO nanosheets, PANI nanofibers, and GO@PANI nanosheets. The diffraction peak of GO at 10.6° can be attributed to the characteristic diffraction peak of GO.^[2] The XRD peaks for GO@PANI at 15.2°, 20.6°, and 25.6°, corresponding to the (011), (020) and (200) crystal planes of pure PANI, suggest that highly crystalline PANI had been successfully produced through interfacial polymerization. Furthermore, the peaks of GO@PANI were almost the same as that of pure PANI. This result reveals that the crystalline structure for PANI can be preserved during employing GO as template in the interfacial approach. Besides, an obvious diffraction peak located at 6.5° for GO@PANI represents greater linearization of polymeric chain and favors electrical conductivity^[3]. The FT-IR spectrum of GO displays a band around 3440 cm⁻¹ due to the -OH stretching mode in -COOH. In comparison with GO, several new peaks for GO@PANI nanosheets appeared, such as the bands at 805, 1135, 1303, 1480, and 1560 cm⁻¹, which can be assigned to the stretching modes of -N-H, -C-H, -C-N, -C=C-, and -C=N, respectively.

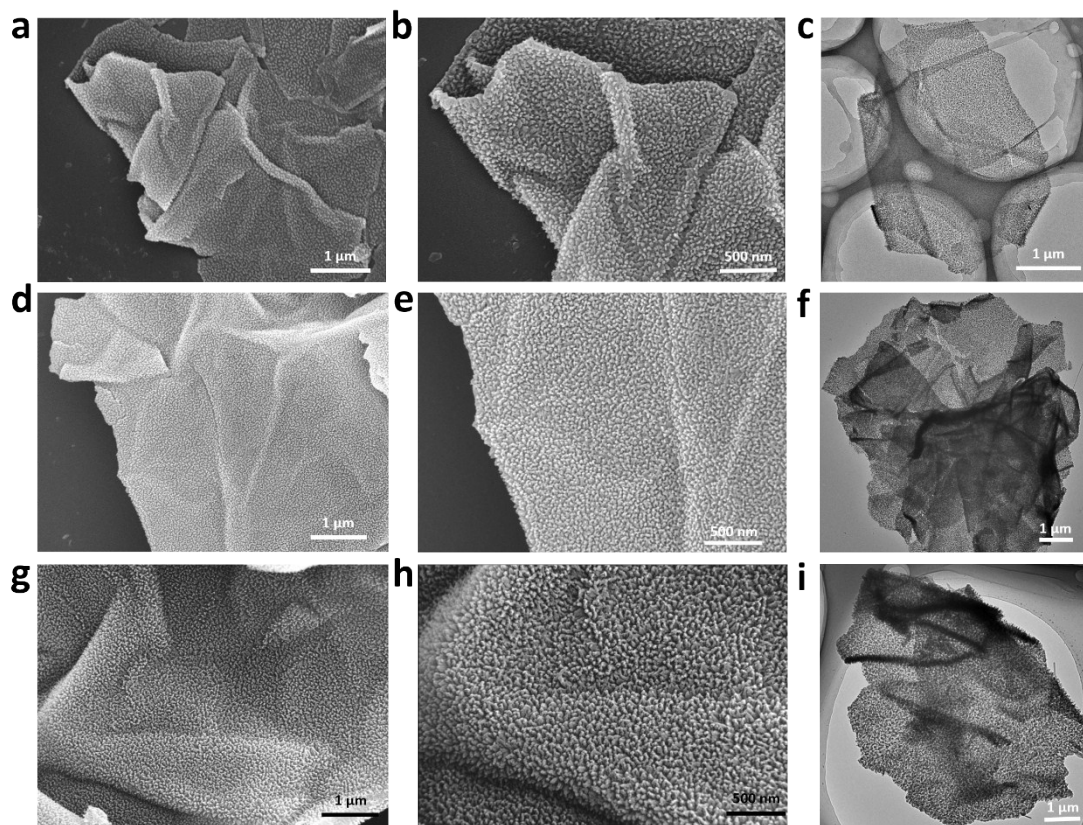


Fig. S4. SEM and TEM images of (a, b, and c) GO@PANI (1:10); (d, e, and f) GO@PANI (1:20); (g, h, and i) GO@PANI (1:40). The 2D morphology of GO@PANI can be well preserved in different GO/aniline weight ratio.

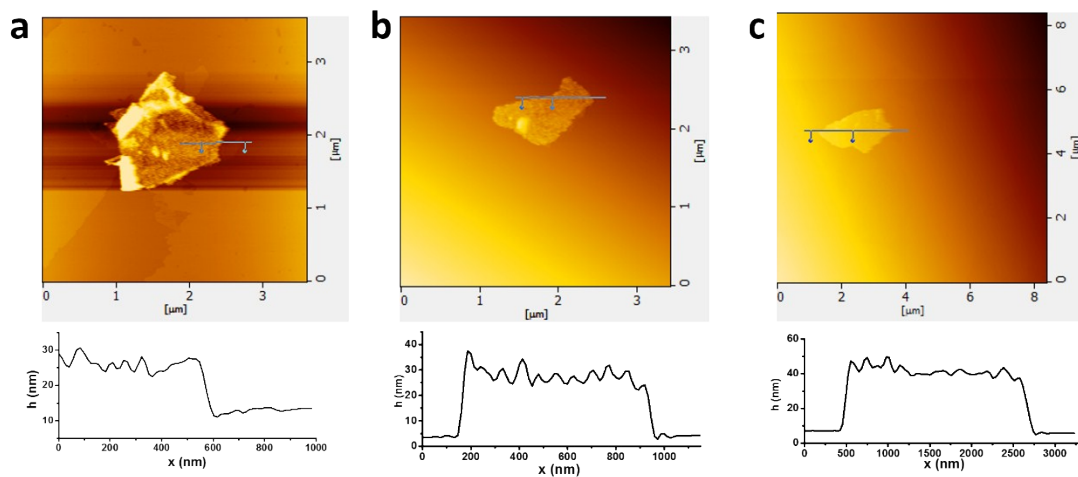


Fig. S5. AFM images of (a) GO@PANI (1:10); (b) GO@PANI (1:20); (c) GO@PANI (1:40). The thicknesses of GO@PANI (1:10), GO@PANI (1:20), and GO@PANI (1:40) were approximately 12 ± 3 , 26 ± 5 , and 36 ± 7 nm, respectively, indicating that the thickness of GO@PANI increases along with the increase of aniline/GO weight ratio.

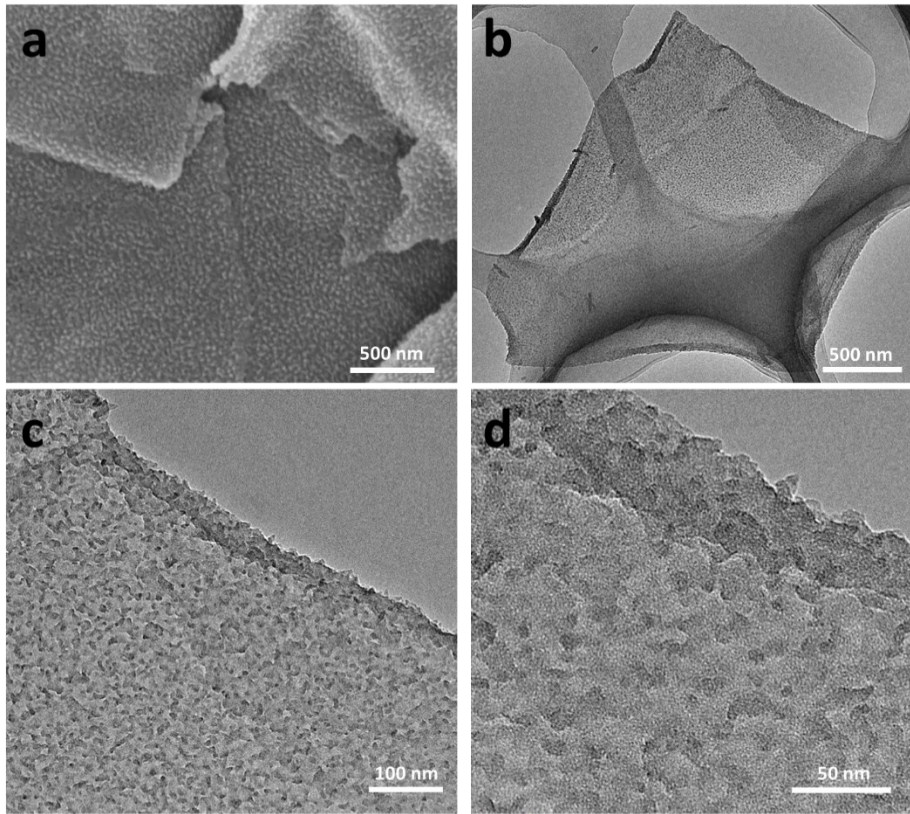


Fig. S6. SEM (a), TEM (b-d) images of GO@(B=PANI) prepared by using H_3BO_3 as the doped acid during the interfacial polymerization.

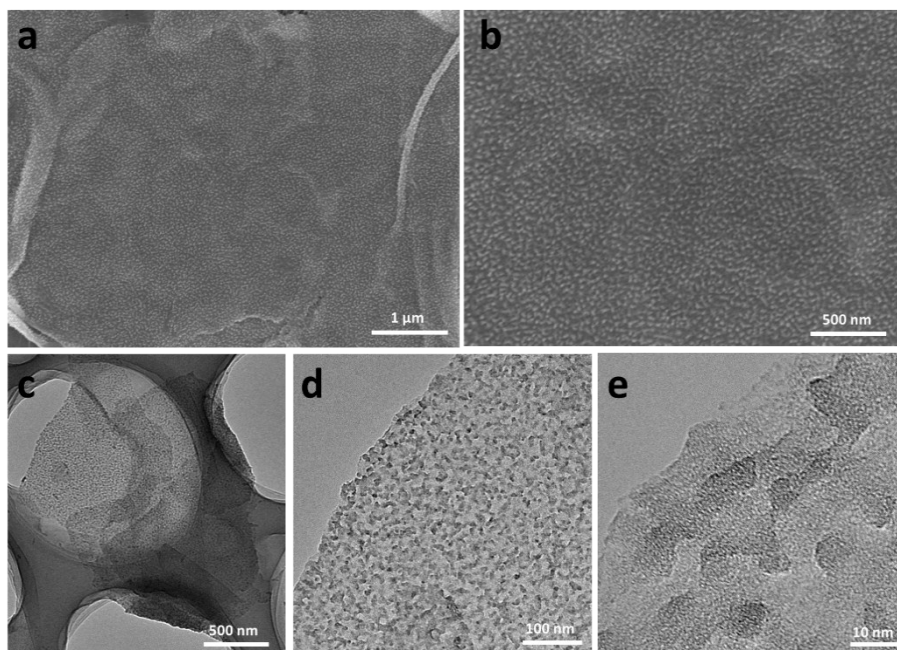


Fig. S7. SEM (a, b) and TEM (c-e) images of GO@(TeCPANI) prepared by using H_6TeO_6 as the doped acid during the polymerization.

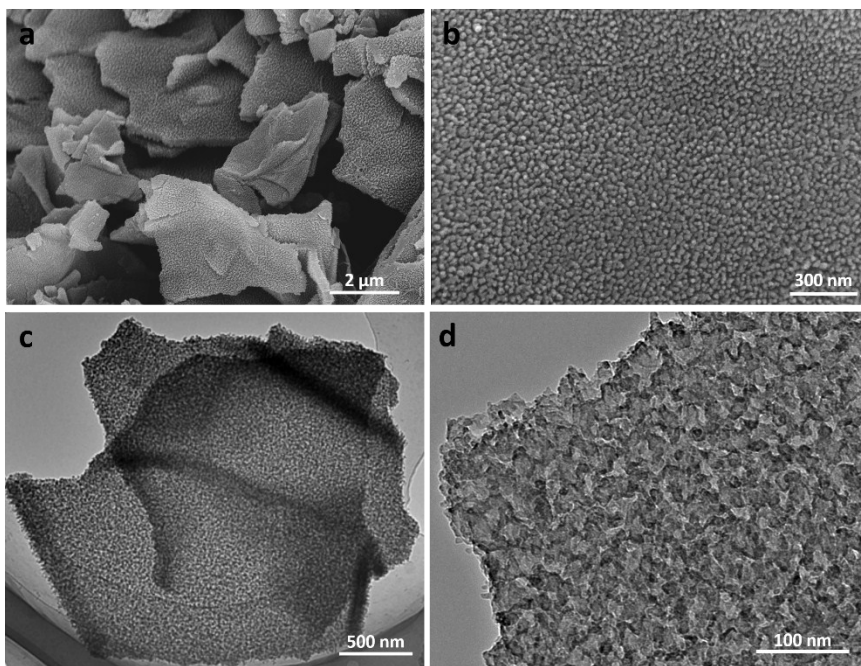


Fig. S8. SEM (a, b) and TEM (c, d) images of GO@(Fe|Pc|PANI). Many free standing and uniform nanosheets can be observed, demonstrating that the 2D morphology can be well preserved by employing H_3PO_4 and FeCl_3 as the dopants.

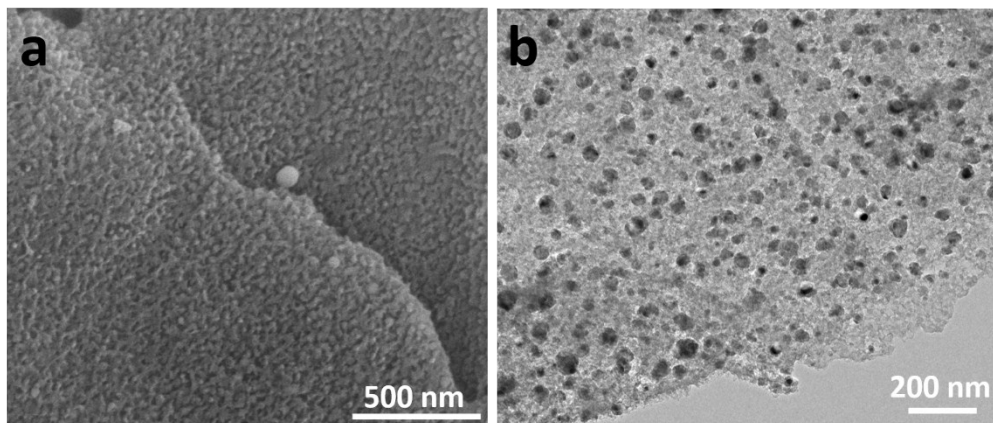


Fig. S9. Enlarged SEM and TEM images of $\text{RG}@\text{(Fe}_2\text{P@NPC)}$. The morphology of PANI domains can be preserved after pyrolysis and the Fe_2P nanoparticles were found uniformly distributed in carbon matrix.

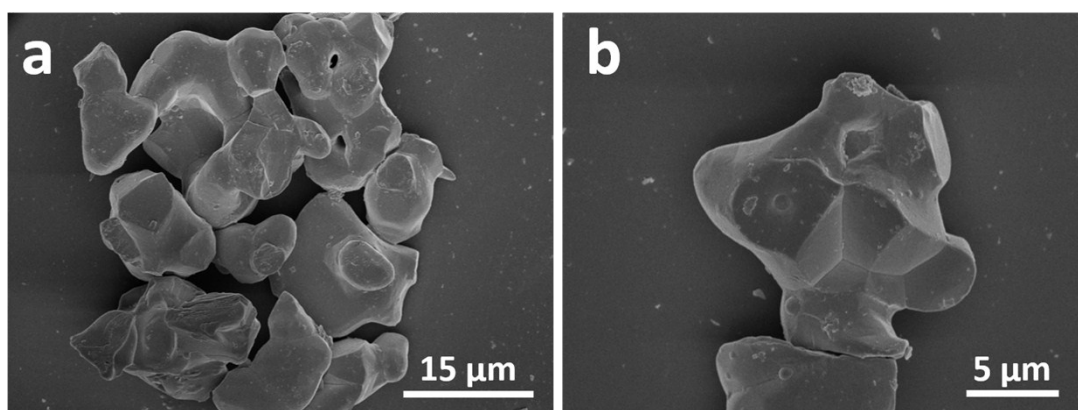


Fig. S10. SEM images of micron-sized Fe_2P particles synthesized by the reduction of the mixture of FeCl_3 and $\text{NH}_4\text{H}_2\text{PO}_4$ at $900\text{ }^\circ\text{C}$ for 2h.

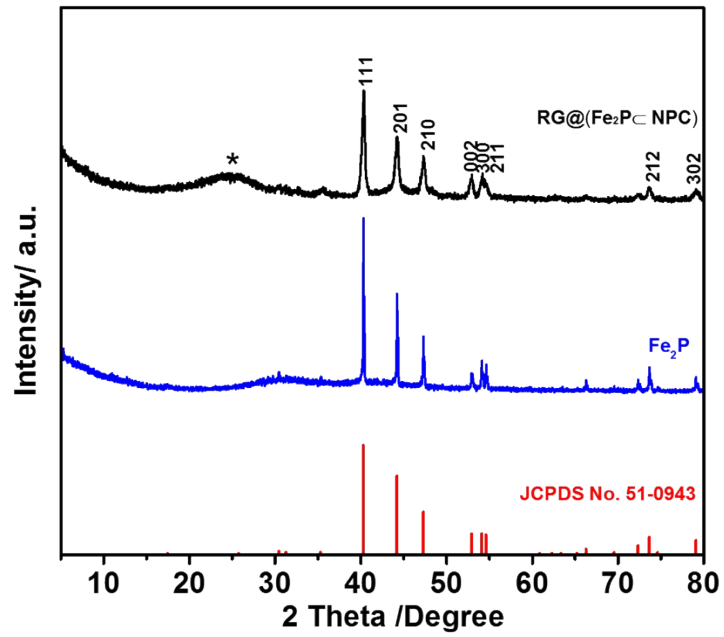


Fig. S11. XRD patterns of RG@(Fe₂P@NPC) (black) and Fe₂P nanoparticles (blue). All XRD peaks can be indexed to crystalline Fe₂P with lattice constants $a=5.867$ Å, $c=3.458$ Å (JCPDS no. 51-0943). Compared to the pure Fe₂P nanoparticles, the diffraction peaks of RG@(Fe₂P@NPC) are more broaden but weaker in intensity, indicating the smaller crystalline size of Fe₂P.^[4] The broad peak (*) at around 26° for RG@(Fe₂P@NPC) can be attributed to the amorphous porous carbon.

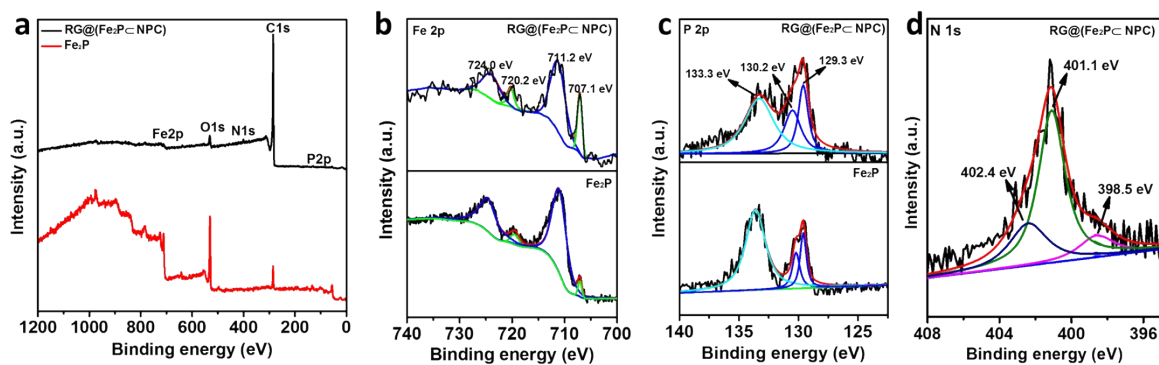


Fig. S12. XPS survey spectra (a), Fe 2p (b), P 2p (c) and N 1s (d) core level spectra for RG@(Fe₂P@NPC) and Fe₂P. The Fe 2p_{3/2} and Fe 2p_{1/2} couple peaks located at 707.1/720.2 eV and 711.2/724.0 eV can be ascribed to Fe₂P and surface-oxidized ion species, respectively. The P 2p_{1/2} and P 2p_{3/2} peaks at 130.2 and 129.3 eV can be attributed to Fe₂P, and the P 2p peak at 133.3 eV can be attributed to residual phosphate. N 1s core level spectrum of RG@(Fe₂P@NPC) can be fitted into 398.5, 401.1 and 402.4 eV, which correspond to the pyridinic N, graphitic N and pyridinic N⁺-O⁻, respectively.^[5]

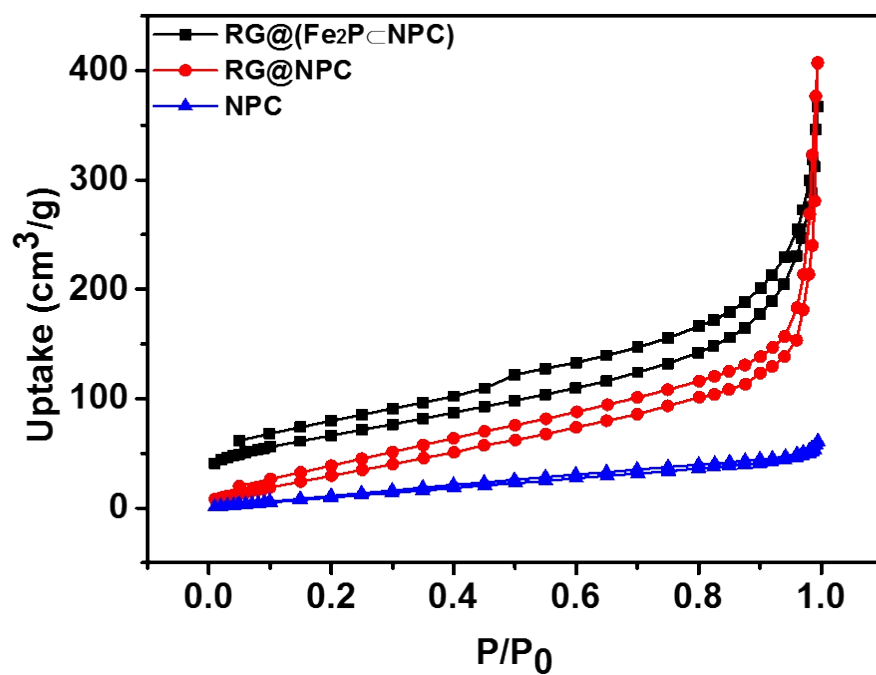


Fig. S13. N₂ sorption isotherms of RG@(Fe₂P@NPC), RG@NPC, and NPC. The BET surface areas of RG@(Fe₂P@NPC), RG@NPC, and NPC are 240, 150 and 69 m² g⁻¹, respectively (Table S2).

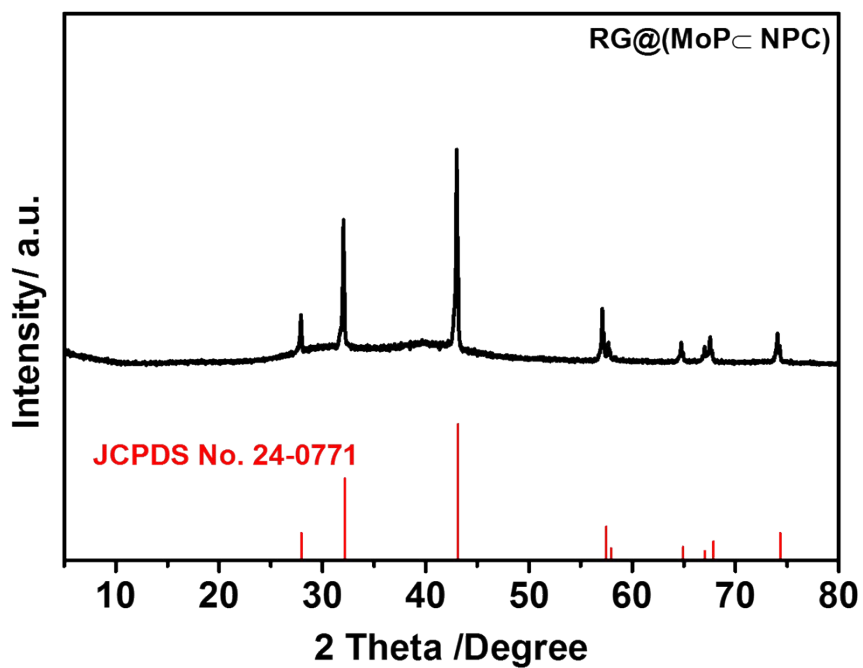


Fig. S14. XRD pattern of RG@(MoP@NPC). All XRD peaks can be indexed to crystalline MoP (JCPDS No. 24-0771).

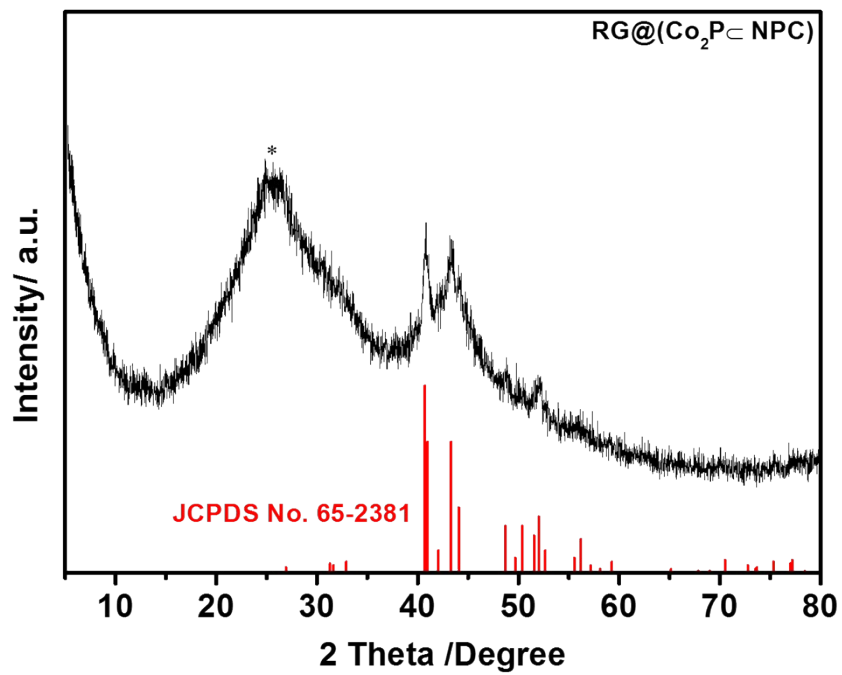


Fig. S15. XRD pattern of RG@(Co₂P@NPC). Key XRD peaks can be indexed to crystalline Co₂P (JCPDS No. 65-2381).

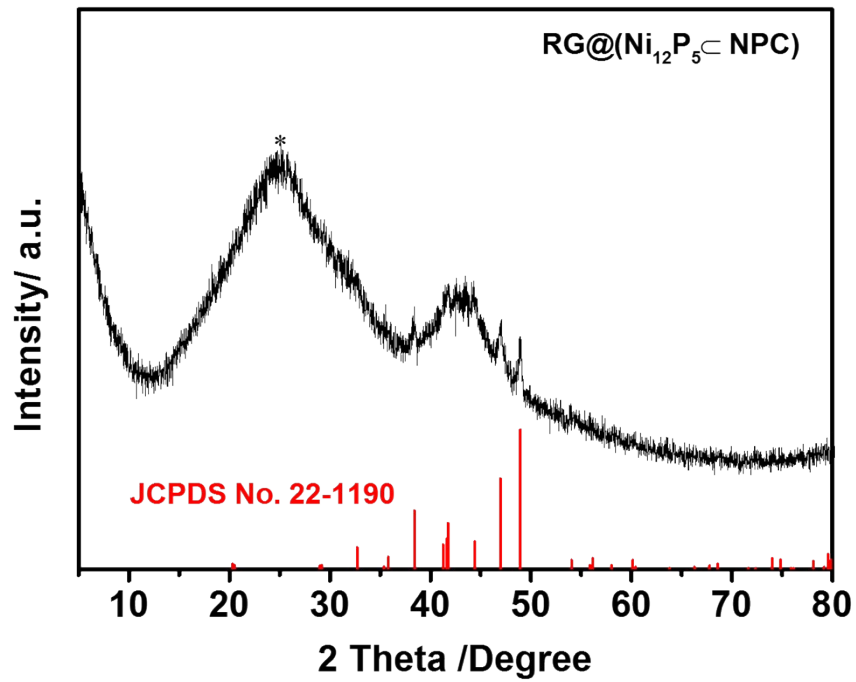


Fig. S16. XRD pattern of RG@(Ni₁₂P₅@NPC). Key XRD peaks can be indexed to crystalline Ni₁₂P₅ (JCPDS No. 22-1190).

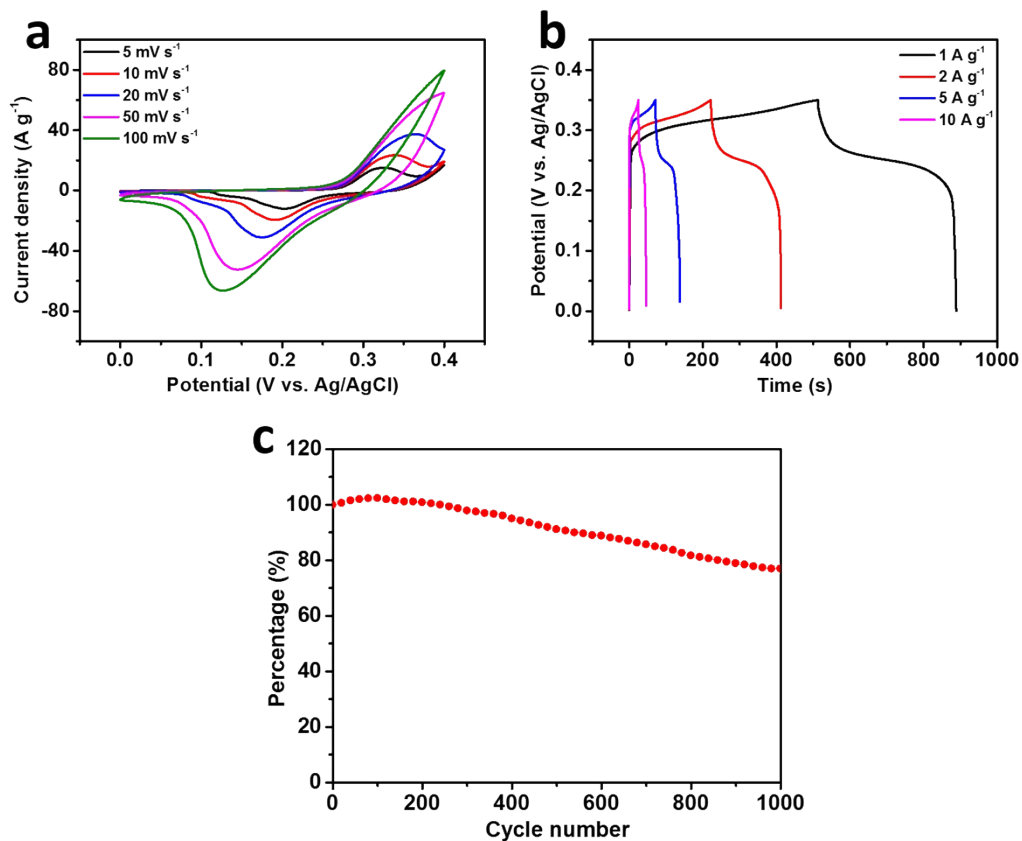


Fig. S17. (a) CV curves of RG@(Fe₂P@NPC) at various scan rates; (b) galvanostatic charge-discharge curves of RG@(Fe₂P@NPC) at a current density of 1-10 A g⁻¹; (c) cycle performance of RG@(Fe₂P@NPC) at the current density of 1 A g⁻¹, exhibiting excellent cycling stability with 77.9% of capacitance retention after 1000 cycles.

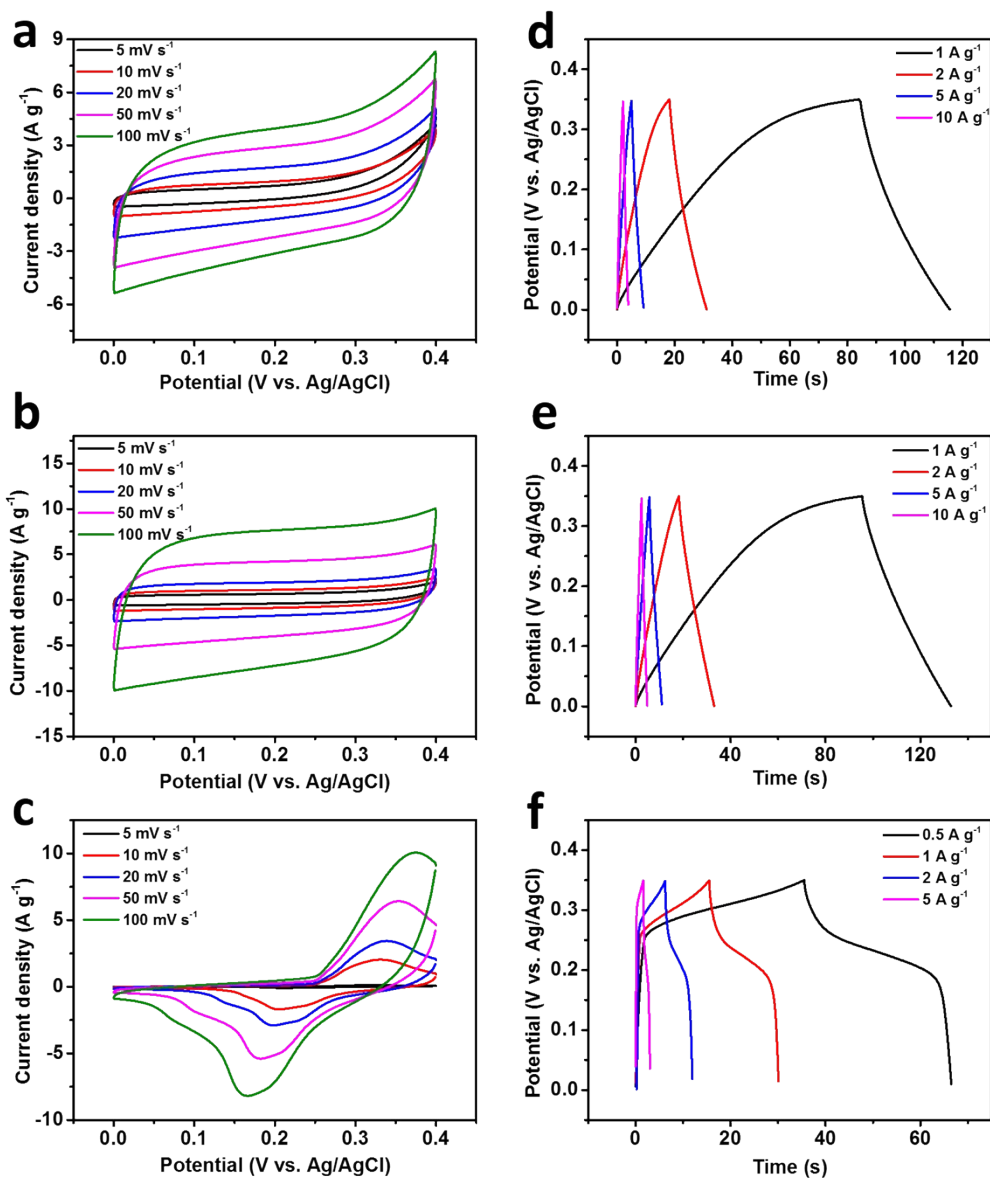


Fig. S18. CV curves for (a) NPC, (b) RG@NPC, (c) Fe_2P nanoparticles at various scan rates from 5 mV s^{-1} to 100 mV s^{-1} ; galvanostatic charge-discharge curves for (d) NPC, (e) RG@NPC, (f) Fe_2P nanoparticles at different current densities.

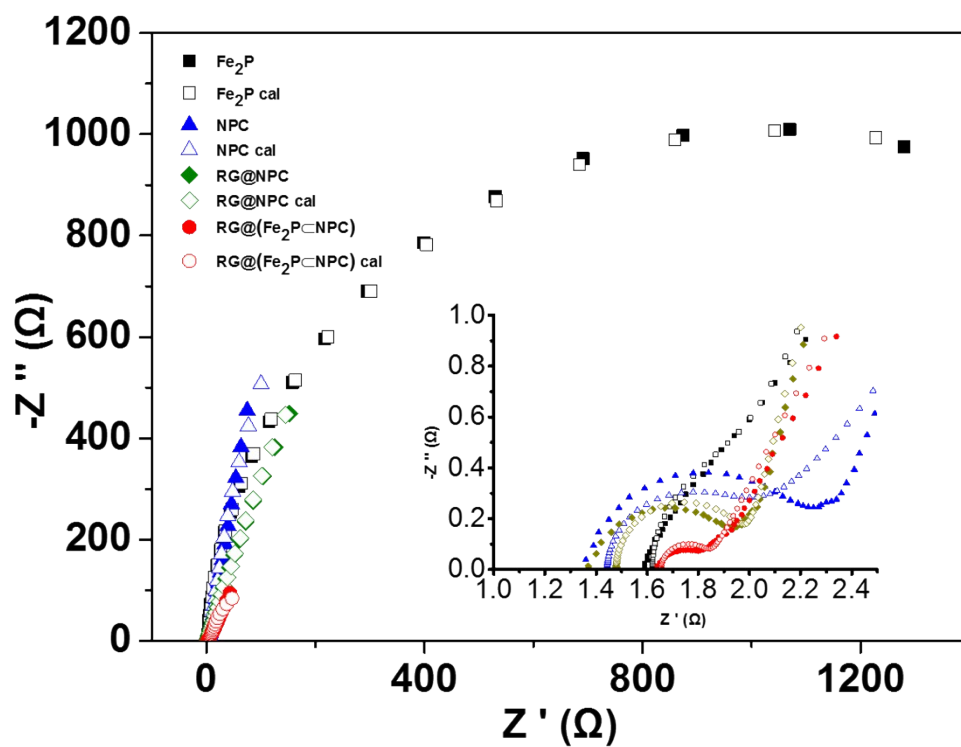


Fig. S19. Nyquist plots of Fe₂P nanoparticles (black), NPC (blue), RG@NPC (green), and RG@(Fe₂P@NPC) (red), (solid: received data; open: calculated data). Inset: magnified Nyquist plot. Below is the equivalent circuit used for fitting of EIS data. According to the equivalent circuit, the charge-transfer resistance values (R_{ct}) of the samples were obtained and summarized in Table S4.

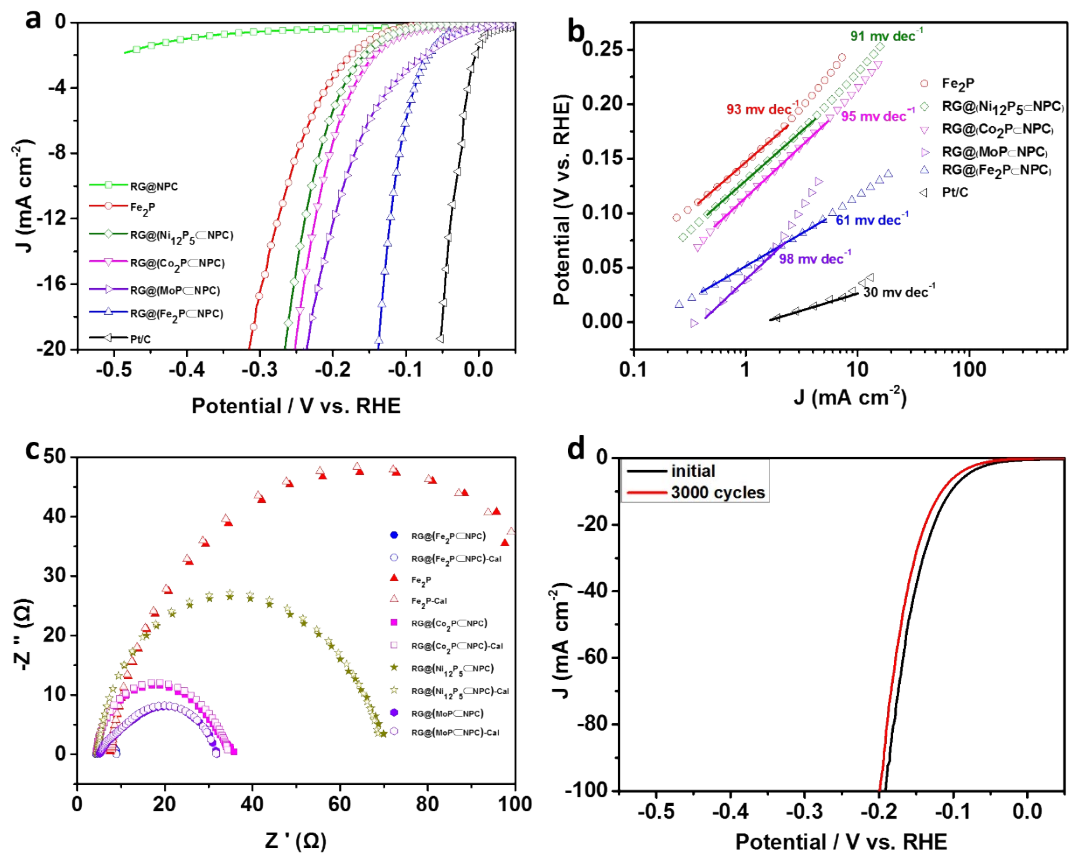


Fig. S20. (a) Polarization curves, (b) Tafel plots and (c) Nyquist plots of as-prepared metal phosphide anchored N-doped porous carbon nanosheets. (d) Cycling stability of the RG@(Fe₂P@NPC) over 3000 scanning cycles in 0.5 M H₂SO₄.

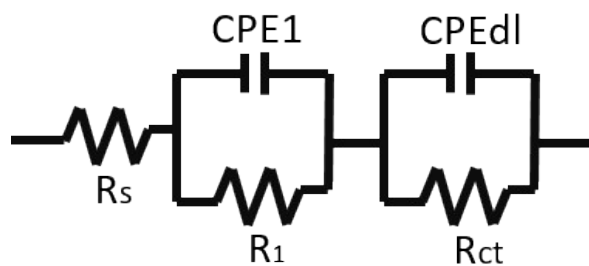


Fig. S21. Equivalent circuit used for fitting of EIS data for HER in 0.5 M H_2SO_4 . R_s is the overall series resistance, $CPE1$ and R_1 are the constant phase element and resistance describing electron transport at materials and GCE interface, $CPEDl$ is the constant phase element of the materials/electrolyte interface, and R_{ct} is the charge transfer resistance at materials/electrolyte interface. The R_{ct} of samples were calculated and summarized in Table S5.

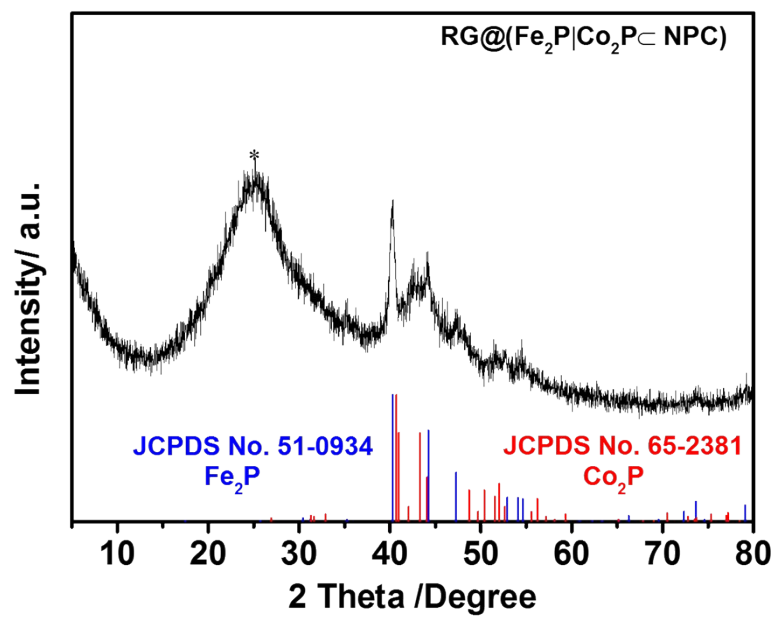


Fig. S22. XRD pattern of RG@(Fe₂P|Co₂P)@NPC nanosheets. Key XRD peaks can be indexed to crystalline Fe₂P (JCPDS No. 51-0934, blue) and crystalline Co₂P (JCPDS No.65-2381, red).

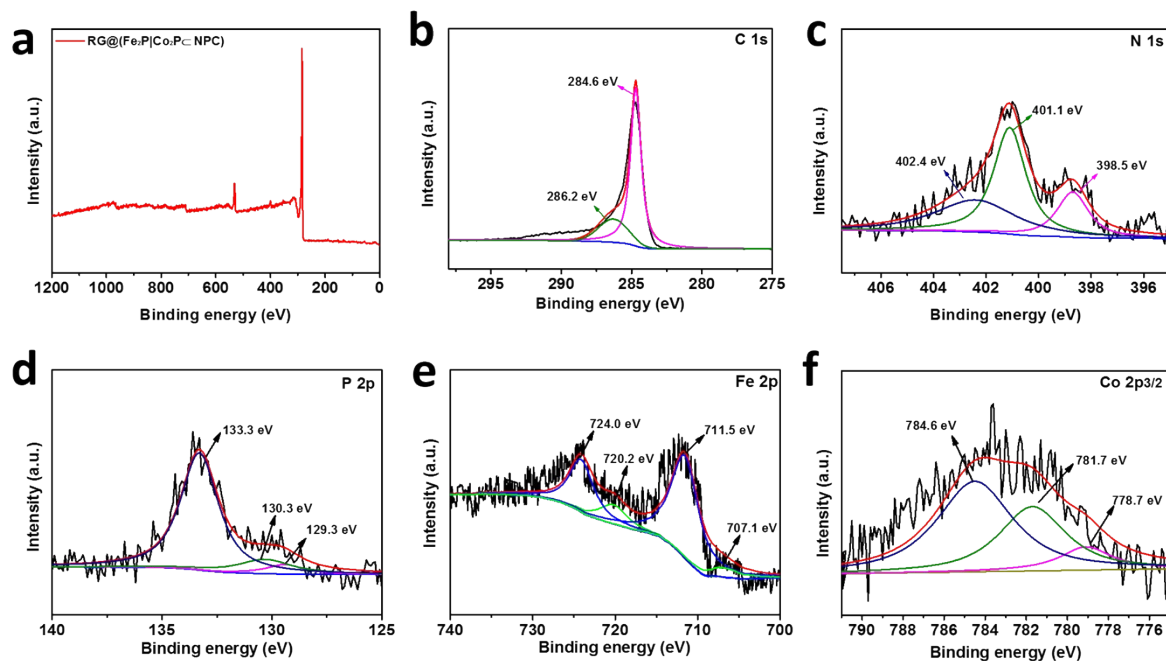


Fig. S23. XPS spectra of $\text{RG}@\text{(Fe}_2\text{P|Co}_2\text{P@NPC)}$. (a) XPS survey spectrum of $\text{RG}@\text{(Fe}_2\text{P|Co}_2\text{P@NPC)}$. (b) C 1s core level spectrum of $\text{RG}@\text{(Fe}_2\text{P|Co}_2\text{P@NPC)}$. The peaks at 284.6 and 286.2 eV can be ascribed to C-C/C=C and C-N, respectively. (c) N 1s core level spectrum of $\text{RG}@\text{(Fe}_2\text{P|Co}_2\text{P@NPC)}$. This spectrum can be fitted into 398.5, 401.1 and 402.4 eV, which correspond to the pyridinic N, graphitic N and pyridinic N⁺-O⁻, respectively.^[5] (d) P 2p core level spectra of $\text{RG}@\text{(Fe}_2\text{P|Co}_2\text{P@NPC)}$. The P 2p_{1/2} and P 2p_{3/2} peaks at 130.3 and 129.3 eV can be attributed to Fe₂P or Co₂P, and the P 2p peak at 133.3 eV can be attributed to residual phosphate. (e) Fe 2p core level spectrum of $\text{RG}@\text{(Fe}_2\text{P|Co}_2\text{P@NPC)}$. The Fe 2p_{3/2} and Fe 2p_{1/2} couple peaks located at 707.1/720.2 eV and 711.5/724.0 eV can be ascribed to Fe₂P and surface-oxidized ion species, respectively. (f) Co 2p_{3/2} spectrum of $\text{RG}@\text{(Fe}_2\text{P|Co}_2\text{P@NPC)}$. The peak located at 778.7 eV suggests that there are reduced Co species in Co₂P. The peaks observed at 781.7 and 784.6 eV could be categorized into an oxidation state of cobalt.^[6]

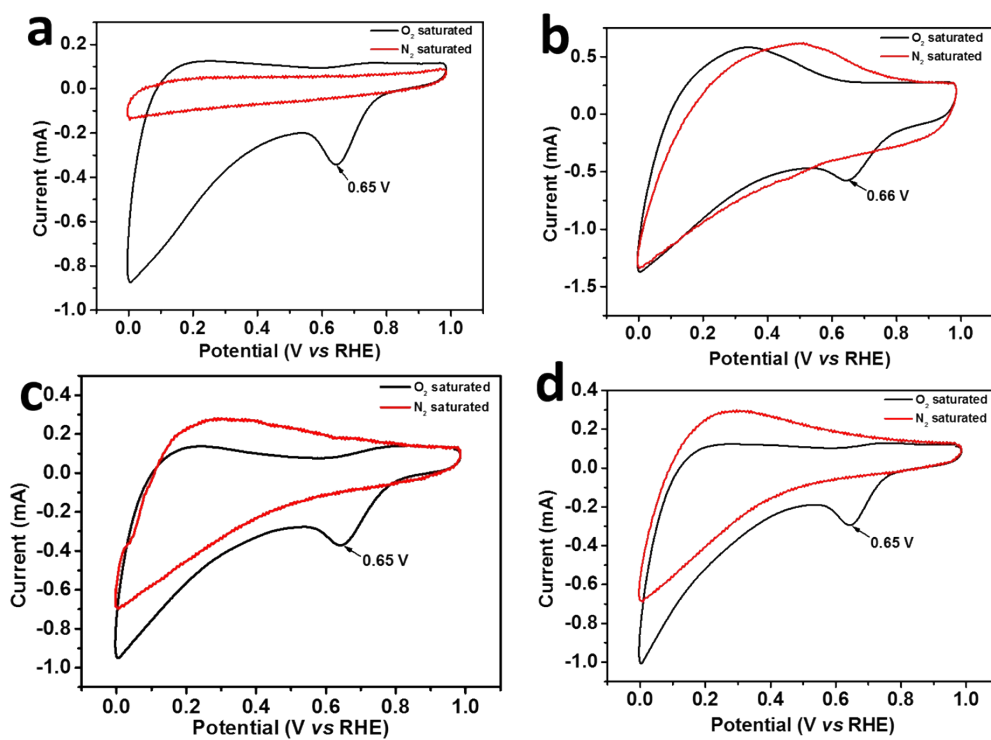


Fig. S24. CV curves for RG@NPC (a), RG@(Fe₂P@NPC) (b), RG@(Co₂P@NPC) (c), and RG@(Ni₁₂P₅@NPC) (d), recorded under nitrogen-saturated (red) and oxygen-saturated (black) 0.1 M KOH solutions.

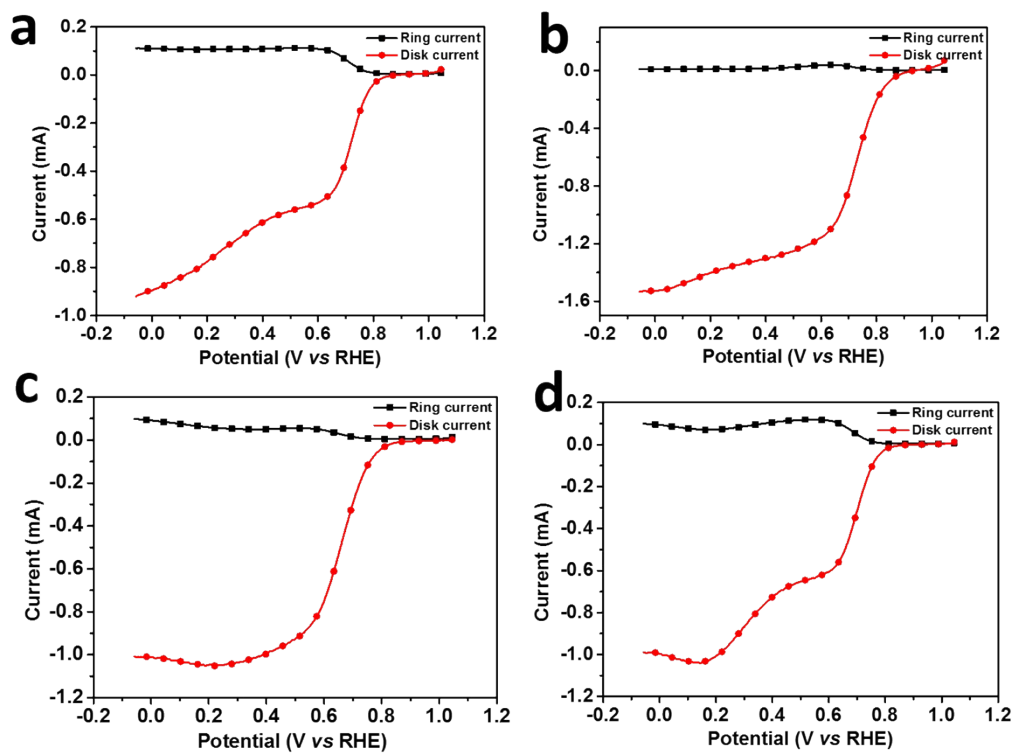


Fig. S25. RRDE curves for RG@NPC (a), RG@(Fe₂P=NPC) (b), RG@(Co₂P=NPC) (c), and RG@(Ni₁₂P₅=NPC) (d) in O₂ saturated 0.1 M KOH solution. All samples were measured at an angular rotation rate of 1600 rpm.

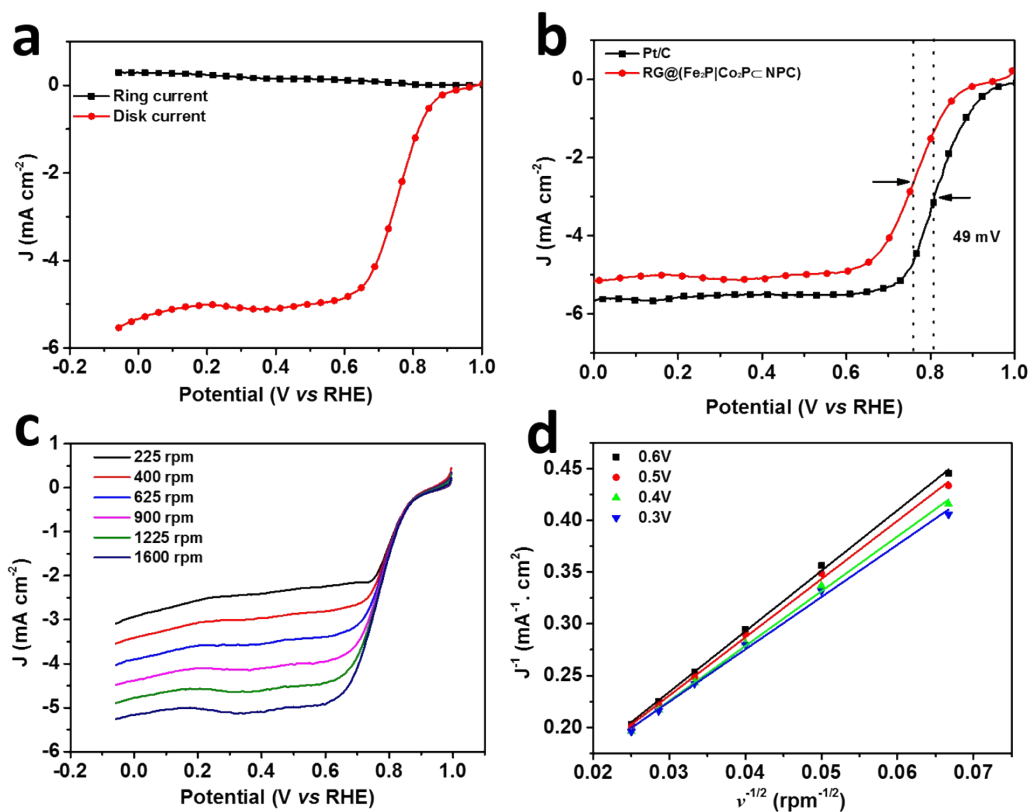


Fig. S26. (a) RRDE current-potential curves for RG@(Fe₂P|Co₂P@NPC) in O₂ saturated 0.1 M KOH solution at an angular rotation rate of 1600 rpm; (b) polarization curves of RG@(Co₂P|Fe₂P@NPC) and Pt/C in O₂-saturated 0.1 M KOH solution. The half-wave potential difference between RG@(Fe₂P|Co₂P@NPC) and Pt/C was found as only 49 mV. (c) RDE voltammograms of RG@(Fe₂P|Co₂P@NPC) recorded in an O₂-saturated 0.1 M KOH solution at a scan rate of 10 mV s⁻¹ at different rotation rates; (d) Koutecky–Levich plots of RG@(Fe₂P|Co₂P@NPC) derived from RDE voltammograms at different electrode potentials.

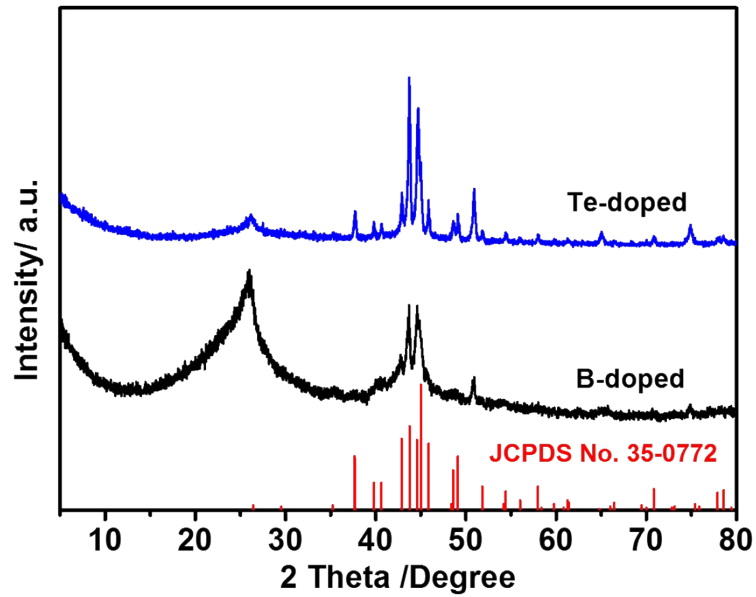


Fig. S27. XRD pattern of RG@(Fe₃C@NPC). Key XRD peaks can be indexed to crystalline Fe₃C (JCPDS No. 35-0772). Blue curve is the Fe₃C anchored Te/N-doped nanosheets (FeCl₃ and H₆TeO₆ as the dopants), and the black curve is the Fe₃C anchored B/N-doped nanosheets (FeCl₃ and H₃BO₃ as the dopants). Therefore, as-developed interfacial method can be used to fabricate metal carbide or other nanoparticles anchored and heteroatom doped carbon nanosheets.

Table S1. Elemental analysis of RG@(Fe₂P⊂NPC) and RG@(Fe₂P|Co₂P⊂NPC) based on XPS results.

sample	C	N	O	P	Fe	Co
	Weight content (%)					
RG@(Fe ₂ P⊂NPC)	85.08	2.59	5.28	3.35	3.71	/
RG@(Fe ₂ P Co ₂ P⊂NPC)	85.33	3.12	5.56	2.25	1.55	2.19

Table S2. N₂ physisorption properties for RG@(Fe₂P⊂NPC), RG@NPC, and NPC.

sample	S _{BET} / (m ² g ⁻¹) ^a	S _{langmuir} / (m ² g ⁻¹) ^b	V _{Tot} / (cm ³ g ⁻¹) ^c	D _{av} / (nm) ^d
RG@(Fe ₂ P⊂NPC)	240	391	0.568	9.4
RG@NPC	150	300	0.630	16.8
NPC	69	362	0.095	5.4

^a Surface area (m² g⁻¹) calculated from the nitrogen sorption isotherms based on the BET model. ^b

Surface area (m² g⁻¹) calculated from the nitrogen sorption isotherms based on the Langmuir model.

^c The total pore volume (cm³ g⁻¹) calculated at P/P₀ = 0.99. ^d Average pore diameter.

Table S3. The selected typical reported supercapacitors based on porous carbons, metal phosphides, oxides and sulfides.

Electrode material	Electrolyte	Specific capacitance	Cycling performance	Reference
PANI/GO	1 M H ₂ SO ₄	555 F/g (1 A/g)	92% (2000 cycles)	[2]
rGO-wrapped MoO ₃	6 M KOH	617 F/g (1 A/g)	87.5% (2000 cycles)	[7]
rGO/ α -MoO ₃	1 M Na ₂ SO ₄	291 F/g (2 mV/s)	/	[8]
N-doped GO	6 M KOH	424 F/g (0.1 A/g)	/	[9]
N-doped rGO	6 M KOH	225 F/g (0.5 A/g)	93% (1000 cycles)	[10]
G-PANI-Co ₃ O ₄	6 M KOH	1063 F/g (0.5 A/g)	95% (2500 cycles)	[11]
MnO ₂ /rGO	1 M Na ₂ SO ₄	217 F/g (0.5 A/g)	84% (1000 cycles)	[12]
P/N doped carbon	6 M KOH	236 F/g (5 mV/s)	86% (5000 cycles)	[13]
WS/rGO	1 M Na ₂ SO ₄	350 F/g (2 mV/s)	10% (1000 cycles)	[14]
NiS/GO	6 M KOH	800 F/g (1 A/g)	87.5% (1000cycles)	[15]
GnP/PANI	1 M H ₂ SO ₄	965.3 F/g (1 A/g)	84.4%(12000cycles)	[16]
RG@(Fe₂P@NPC)	6 M KOH	1098 F/g (1 A/g)	77.9% (1000 cycles)	This work

Table S4. The charge-transfer resistance values (R_{ct}) of the samples as electrodes of supercapacitors in 6 M KOH.

sample	R_{ct} (Ω)
RG@(Fe ₂ P@NPC)	0.25
RG@NPC	0.45
NPC	0.61
Fe ₂ P nanoparticles	1032

Table S5. The R_{ct} of as-prepared MPs-base carbon nanosheets as electrochemical catalysts for hydrogen evolution reaction in 0.5 M H_2SO_4 .

sample	R_{ct} (Ω)
RG@(Fe ₂ P \subset NPC)	0.602
RG@(MoP \subset NPC)	3.872
RG@(Co ₂ P \subset NPC)	5.992
RG@(Ni ₁₂ P ₅ \subset NPC)	35.11
Fe ₂ P nanoparticles	111.3

Table S6. Comparison of HER performance in acid media for as-prepared MPs-based catalysts.

catalyst	Tafel slope (mV \cdot dec ⁻¹)	η at 10 mA cm ⁻² (mV)	η at 20 mA cm ⁻² (mV)
RG@(Fe ₂ P \subset NPC)	61	115	140
RG@(MoP \subset NPC)	98	186	235
RG@(Co ₂ P \subset NPC)	95	213	252
RG@(Ni ₁₂ P ₅ \subset NPC)	91	229	265
Fe ₂ P nanoparticles	93	260	316

Table S7. Comparison of HER performance in acid media for RG@(Fe₂P⊂NPC) with reported HER electrocatalysts.

catalyst	Tafel slope (mV·dec ⁻¹)	η at 10 mA cm ⁻² (mV)	η at 20 mA cm ⁻² (mV)	reference
FeP@PC	49	52	98	[17]
MoP	54	140	/	[18]
MoP-CA2	54	125	160	[19]
CoP	/	75	85	[20]
CoP/CNT	76	128	175	[21]
Co ₂ P nanorods	71	134	167	[6]
Co-NRCNTs	80	260	/	[22]
Ni ₂ P	81	117	130	[23]
Ni ₃ P ₄	40	140	/	[24]
FeP nanosheets	67	240	300	[25]
FeSe ₂	66	/	/	[26]
Fe ₂ P/NGr	65	138	164	[27]
RG@(Fe₂P⊂NPC)	61	115	140	This work

Reference:

- [1] W. S. Hummers Jr, R. E. Offeman, *J. Am. Chem. Soc.*, 1958, **80**, 1339-1339.
- [2] J. Xu, K. Wang, S.-Z. Zu, B.-H. Han, Z. Wei, *ACS Nano*, 2010, **4**, 5019-5026.
- [3] C. Xing, Z. Zhang, L. Yu, L. Zhang, G. A. Bowmaker, *RSC Adv.*, 2014, **4**, 32718-32725.
- [4] Y.-X. Wang, J. Yang, S.-L. Chou, H. K. Liu, W.-x. Zhang, D. Zhao, S. X. Dou, *Nat. Commun.*, 2015, **6**.
- [5] W. Wei, H. Liang, K. Parvez, X. Zhuang, X. Feng, K. Müllen, *Angew. Chem., Int. Ed.*, 2014, **126**, 1596-1600.
- [6] Z. Huang, Z. Chen, Z. Chen, C. Lv, M. G. Humphrey, C. Zhang, *Nano Energy*, 2014, **9**, 373-

- [7] K. Yuan, Y. Xu, J. Uihlein, G. Brunklaus, L. Shi, R. Heiderhoff, M. Que, M. Forster, T. Chassé, T. Pichler, *Adv. Mater.*, 2015, **27**, 6714-6721.
- [8] J. Chang, M. Jin, F. Yao, T. H. Kim, V. T. Le, H. Yue, F. Gunes, B. Li, A. Ghosh, S. Xie, *Adv. Funct. Mater.*, 2013, **23**, 5074-5083.
- [9] X. Zhuang, F. Zhang, D. Wu, X. Feng, *Adv. Mater.*, 2014, **26**, 3081-3086.
- [10] Z. Lei, L. Lu, X. Zhao, *Energy Environ. Sci.*, 2012, **5**, 6391-6399.
- [11] S. Li, D. Wu, C. Cheng, J. Wang, F. Zhang, Y. Su, X. Feng, *Angew. Chem., Int. Ed.*, 2013, **125**, 12327-12331.
- [12] A. Sumboja, C. Y. Foo, X. Wang, P. S. Lee, *Adv. Mater.*, 2013, **25**, 2809-2815.
- [13] U. B. Nasini, V. G. Bairi, S. K. Ramasahayam, S. E. Bourdo, T. Viswanathan, A. U. Shaikh, *J. Power Sources*, 2014, **250**, 257-265.
- [14] S. Ratha, C. S. Rout, *ACS Appl. Mater. Inter.*, 2013, **5**, 11427-11433.
- [15] A. Wang, H. Wang, S. Zhang, C. Mao, J. Song, H. Niu, B. Jin, Y. Tian, *Appl. Surf. Sci.*, 2013, **282**, 704-708.
- [16] M. Moussa, M. F. El-Kady, H. Wang, A. Michimore, Q. Zhou, J. Xu, P. Majeswki, J. Ma, *Nanotechnology*, 2015, **26**, 075702.
- [17] S. Han, Y. Feng, F. Zhang, C. Yang, Z. Yao, W. Zhao, F. Qiu, L. Yang, Y. Yao, X. Zhuang, *Adv. Funct. Mater.*, 2015, **25**, 3899-3906.
- [18] P. Xiao, M. A. Sk, L. Thia, X. Ge, R. J. Lim, J.-Y. Wang, K. H. Lim, X. Wang, *Energy Environ. Sci.*, 2014, **7**, 2624-2629.
- [19] Z. Xing, Q. Liu, A. M. Asiri, X. Sun, *Adv. Mater.*, 2014, **26**, 5702-5707.
- [20] J. Wang, W. Cui, Q. Liu, Z. Xing, A. M. Asiri, X. Sun, *Adv. Mater.*, 2016, **28**, 215-230.
- [21] Q. Liu, J. Tian, W. Cui, P. Jiang, N. Cheng, A. M. Asiri, X. Sun, *Angew. Chem., Int. Ed.*, 2014, **126**, 6828-6832.
- [22] X. Zou, X. Huang, A. Goswami, R. Silva, B. R. Sathe, E. Mikmeková, T. Asefa, *Angew. Chem., Int. Ed.*, 2014, **126**, 4461-4465.
- [23] E. J. Popczun, J. R. McKone, C. G. Read, A. J. Biacchi, A. M. Wiltrout, N. S. Lewis, R. E. Schaak, *J. Am. Chem. Soc.*, 2013, **135**, 9267-9270.
- [24] M. Ledendecker, S. Krick Calderón, C. Papp, H. P. Steinrück, M. Antonietti, M. Shalom,

Angew. Chem., Int. Ed., 2015, **127**, 12538-12542.

[25] Y. Xu, R. Wu, J. Zhang, Y. Shi, B. Zhang, *Chem. Commun.*, 2013, **49**, 6656-6658.

[26] D. Kong, J. J. Cha, H. Wang, H. R. Lee, Y. Cui, *Energy Environ. Sci.*, 2013, **6**, 3553-3558.

[27] Z. Huang, C. Lv, Z. Chen, Z. Chen, F. Tian, C. Zhang, *Nano Energy*, 2015, **12**, 666-674.